Urban Climate 44 (2022) 101218

Contents lists available at ScienceDirect

Urban Climate

journal homepage: www.elsevier.com/locate/uclim

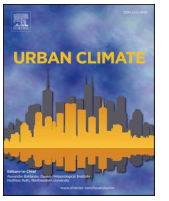

Lisbon urban heat island in future urban and climate scenarios

Rui Silva [a,*], Ana Cristina Carvalho [b], Susana Cardoso Pereira [a], David Carvalho [a], Alfredo Rocha [a]

[a] Department of Physics and Centre for Environmental and Marine Studies (CESAM) Campus Universitário de Santiago, University of Aveiro, 3810-093 Aveiro, Portugal

[b] Swedish Meteorological and Hydrological Institute, SMHI FoUmmk, 601 76 Norrköping, Sweden

ARTICLE INFO

Keywords:
Urban heat islands
Climate change
WRF
Lisbon

ABSTRACT

Urban heat Islands (UHIs) may constitute a hazard for urban populations, particularly under extreme events such as heatwaves. Lisbon is a medium-size city regularly affected by heatwaves with maximum temperatures >35 °C and is expected to grow and densify during this century.

This study evaluates the UHI in the Municipality of Lisbon (ML) for the heatwave with the highest maximum average temperature identified in long-term (2081–2100) RCP8.5 scenario climate simulations, relative to present conditions, represented by a typical heatwave identified in historical (1986–2005) period climate simulations. The expected future consolidation of the city (up to 2100) is considered, as well as the anthropogenic heat and irrigation effects. Simulations are performed with the Weather Research and Forecasting model (WRF) coupled with the Single-layer Urban Canopy Model (SLUCM). The results reveal that urban irrigation effects compensate anthropogenic heat due to increased latent heat release. The expected city consolidation up to 2100 produces the largest increase in the UHI intensity (UHII) during nighttime due to the introduction of urban land use land cover (LULC) with reduced green fraction. No evidence of synergistic interactions between UHI and heatwave intensities were found, with the UHII mostly depending on wind direction and intensity.

1. Introduction

The underlying LULC of a surface will determine the heat and water budgets between the surface and the atmosphere (Yang et al., 2015). Among other impacts, any change on the LULC, such as urban artificial surfaces, can alter these budgets and, consequently, the atmosphere characteristics expressed by weather conditions and urban climatology (a short description is available in Harman and Belcher, 2006 and a comprehensive one in Oke et al., 2017). These changes can be felt at local and regional levels, depending on the scale of the modification and physical properties of the new LULC. Along with buildings' dimensions and city planning, these are some of the elements that, according to Oke et al. (2017), are included in the urban form set of features.

However, the way urban environments function also has an impact in the urban atmosphere. According to Oke (1988) and Oke et al. (2017), the heat released from anthropogenic sources, embedded in the way a specific urban environment works, is adding to the UHI effect. The main sources of anthropogenic heat are considered to be the heat released by the human metabolism, the heat from vehicles, and the internal heat of buildings - which includes the heat released by electrical equipment (e.g., air conditioning) as well as

* Corresponding author at: Department of Physics and Centre for Environmental and Marine Studies (CESAM), University of Aveiro, Portugal.
E-mail address: ruipedrosilva@ua.pt (R. Silva).

https://doi.org/10.1016/j.uclim.2022.101218
Received 20 December 2021; Received in revised form 31 May 2022; Accepted 19 June 2022
Available online 24 June 2022

the heat from fossil fuels burning for heating (Sailor et al., 2016; Sailor and Lu, 2004).

The heat released by human activities is considered one waste by-product of the metabolic cycle of an urban environment (Oke et al., 2017). Hence, the release of anthropogenic heat is dependent on the population density, the climate of each region, the season and time of day. As an example, Ichinose et al. (1999) showed the importance of the human activity sectors and the seasonal influence of the anthropogenic heat emission on the temperature environment over Tokyo. Thus, the combined effect of several heat sources inside a specific urban environment will impact differently the urban boundary layer (UBL) and all the planetary boundary layer (PBL). These sources are those having a direct impact on the atmosphere, and they will be one of the main focuses of the present work.

There are several methods to study urban meteorology and climatology. Numerical modelling is the one that allows a complete experimental control on the factors that can determine the interaction between the form and function of a specific urban canopy, PBL, and all the scales involved in a specific urban climate (Oke et al., 2017). That is the reason why so much effort has been dedicated to improve the UBL description leading to urban canopy parameterizations and anthropogenic heat release schemes inside numerical weather prediction (NWP) models like the WRF (see https://ral.ucar.edu/solutions/products/urban-canopy-model and references within).

Ruiting and Han (2016) showed the importance that the combined effects of considering the local diurnal hourly scaling factors of anthropogenic heat release of Beijing and the WRF's SLUCM have on several atmospheric parameters near the surface and on the PBL height. Using WRF model simulations coupled with an urban canopy model, Feng et al. (2012) studied the impacts resulting from changes in urbanization as well as the release of anthropogenic heat in five of China's most populous regions over a two-year period (December 2006 to December 2008). The results show that the combined effect of changes in urbanization and anthropogenic heat can lead to a temperature increase up to 2 °C in some regions, and to a considerable decrease in the albedo and soil moisture. In another study carried out by Yang and Wang (2015) for the city of Phoenix, USA, the impact of various irrigation schemes coupled to an urban canopy model was tested. The study concludes that the application of different irrigation schemes increases the moisture available for evapotranspiration and decreases the surface temperature, which can exceed 3 °C during the summer period compared to the case where no irrigation scheme is used.

In one hand, the WRF model is a valuable tool to assess changes in the synoptic weather due to changes in the global climate (under different emissions scenarios) and how those changes can influence the urban climate. On the other hand, it can also be used on the evaluation of certain mitigation and/or adaptation measures that may be part of a specific urban environment under future climate scenarios (Fallmann et al., 2014; Li et al., 2018; Warrach-Sagi et al., 2018).

The work here presented makes use of the WRF model to evaluate the UHI in Lisbon for future climate scenarios considering mixing aspects of the form and function of the city. Regarding its form, the expected evolution of the city within the limits of the ML is considered through the inclusion of the urban LULC areas to be consolidated by 2050 and 2100. Regarding the functions, the study also considers the effects of anthropogenic heat and irrigation on the green fraction of urban LULC classes.

Section 2 of the present paper explores the data and methods applied in the model setup and its description; the specificities of the anthropogenic heat emitted by the city of Lisbon and how the WRF model was adjusted to include it; the description of the irrigation scheme; the considerations about the surface energy balance in the WRF/Noah LSM/SLUCM modelling system; and how the present and future LULC of the city is described in WRF. In Section 3 the results are discussed and, finally, Section 4 holds the final remarks and conclusions of the work.

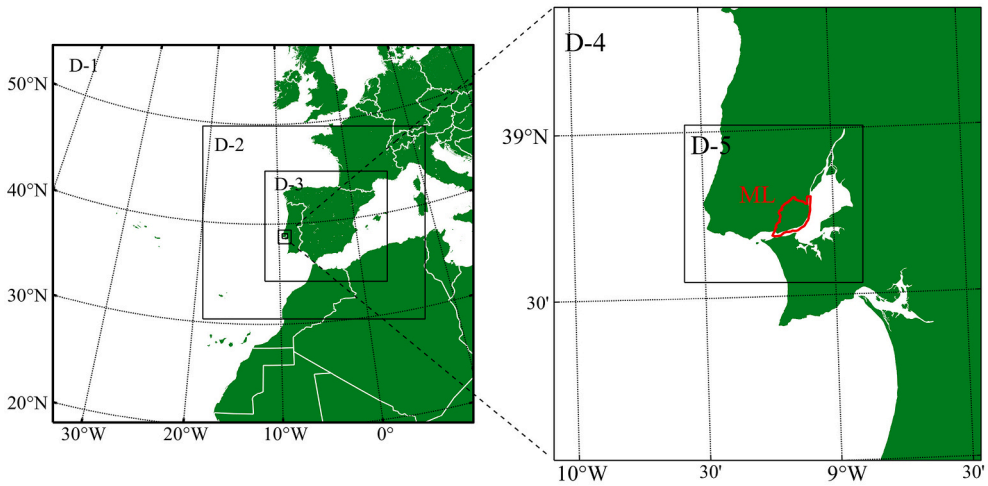

Fig. 1. Domains' configuration used in the climatic (D-1, D-2, and D-3) and urban heat island (D-1, D-2, D-3, D-4, and D-5) simulations. The area delimited by the red contour represents the Municipality of Lisbon (ML), within which the white color represents the public water domain. (For interpretation of the references to color in this figure legend, the reader is referred to the web version of this article.)

2. Materials and methods

2.1. Model setup and description

2.1.1. Climatic simulations and heatwaves' selection

To carry out UHI simulations under future urban and climate scenarios, two sets of regional climatic simulations were performed using the WRF version 3.9 (Skamarock et al., 2008) with the modifications introduced by Fita et al. (2010). The first simulation represents the historical (HIST) past-present climate that extends for a 20-year period, from 1986 to 2005, while the second simulation corresponds to the long-term future scenario (LONG), from 2081 to 2100. To force the model in what is related to the initial and boundary conditions, outputs of the global climate model (GCM), MPI-ESM (LR), from the Max-Plank Institute were used (available at: CERA - WDCC (dkrz.de)) (Giorgetta et al., 2013). The retrieved GCM data is from the r1i1p1 initialization and RCP8.5 scenario, with a horizontal resolution of 1.9° × 1.9° in 47 hybrid sigma-pressure levels and provided to WRF with six-hourly frequency. The preference for the RCP8.5 scenario is due to the fact that this is the most extreme among the available Representative Concentration Pathways (RCPs) scenarios, that projects an increasing radiative forcing peaking at 8.5 W m^{-2} by the end of the 21st century due to greenhouse gases emissions. A model configuration of three nested domains with horizontal grid spacing of 81 km, 27 km, and 9 km (respectively, D-1, D-2, and D-3 in Fig. 1) was implemented. This dynamical downscaling and model configuration follows the one described in Marta-Almeida et al. (2016) except for the number of vertical levels and the choice of the PBL scheme. As Marta-Almeida et al. (2016), sea surface temperature update was used and spectral-nudging was applied in D-1 for wavelengths larger than 1000 km (Miguez-Macho et al., 2004). A two-way nesting strategy was applied, with the model top defined at 50 hPa. A total of 46 vertical levels were used with the first model level defined at ~56 m for consistency with the UHI simulations performed by Silva et al. (2021) for the Lisbon Metropolitan Area. Due to the importance of accurate LULC and topography representation in the WRF model, the Coordination on the Environment (CORINE) LULC (Büttner, 2014) for the year of 2012 (hereinafter referred to as "CLC2012") and the NASA's Shuttle Radar Topography Mission (SRTM) (Farr et al., 2007), with a horizontal resolution of ~100 m and ~90 m, respectively, were used. These two geographical datasets are shown in Fig. 2 and Fig. 3, respectively, for the highest resolution domain of the UHI simulations described in the following section (Section 2.1.2). The procedure to include the CLC2012 LULC and SRTM topography data in WRF's modelling system is the same as the one described in Section 2.1.1 of Silva et al. (2021). WRF's model physical parameterizations include the WRF-Single-Moment 6-class microphysics (WSM6) scheme (Hong and Lim, 2006), the Dudhia shortwave radiation scheme (Dudhia, 1989), the Rapid Radiative Transfer Model (RRTM) longwave radiation model (Mlawer et al., 1997), the Revised MM5 surface model (Jiménez et al., 2012), the BouLac planetary boundary layer model (Bougeault and Lacarrere, 1989), the

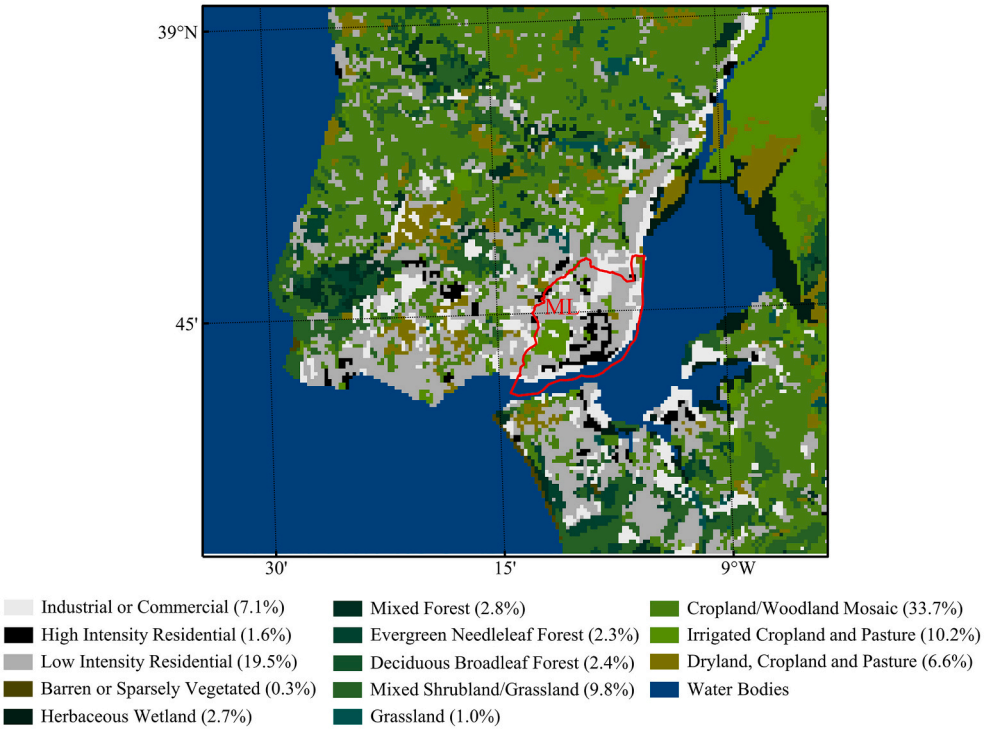

Fig. 2. Model LULC with percentage of area of each LULC class in domain D-5. The area delimited by the red contour represents the Municipality of Lisbon (ML), within which blue color represents the public water domain. (For interpretation of the references to color in this figure legend, the reader is referred to the web version of this article.)

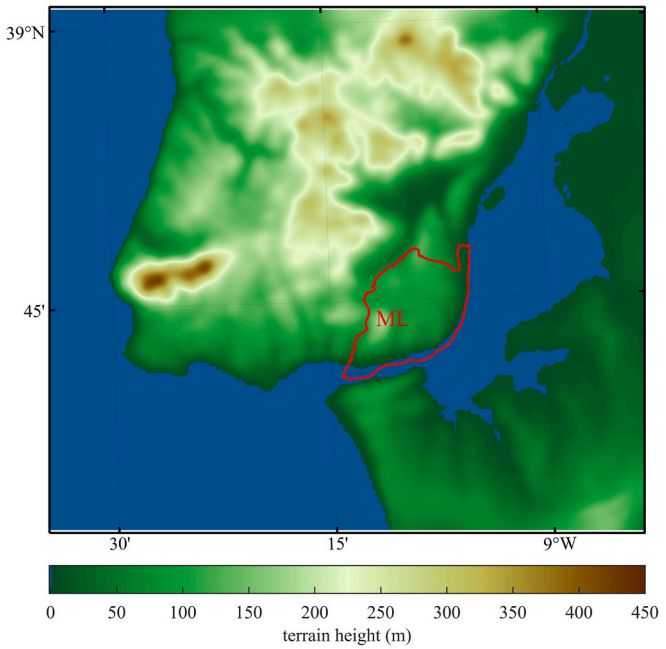

Fig. 3. Model LULC with percentage of area of each LULC class in domain D-5. The area delimited by the red contour represents the Municipality of Lisbon (ML), within which blue color represents the public water domain. (For interpretation of the references to color in this figure legend, the reader is referred to the web version of this article.)

Noah Land Surface Model (Noah LSM) (Chen and Dudhia, 2001), and the Grell-Freitas cumulus scheme (Grell and Freitas, 2014).

A similar methodology to the one used by Rocha et al. (2020) was applied for heatwave identification. Two heatwaves were selected from the HIST and LONG climatic periods. The heatwave identified in HIST period has a relatively short duration (4 days) and low mean maximum temperature, while the heatwave selected in the LONG period is the most intense one (i.e., heatwave with the highest mean maximum temperature) identified in the climatic simulations of this period, having a duration of 10 days.

2.1.2. Urban heat island simulations

The numerical simulations of the ML's UHI were performed using the same physical parameterizations, LULC, topography, and initial and boundary conditions of the climatic simulations described in Section 2.1.1. Two additional domains with a horizontal grid spacing of 1 km and 333 m (respectively, D-4 and D-5 in Fig. 1) were added to the domains' configuration of the climatic simulations to proceed with the dynamical downscaling of the MPI-ESM (LR) data to the Lisbon Metropolitan Area, and to perform the UHI simulations during the heatwaves selected from the HIST and LONG climatic simulations. Hence, the UHI simulations considered a total of five nested domains and were performed in two-way nesting mode. The updated LULC and the percentage of coverage of each LULC class is shown in Fig. 2, for domain D-5, while the updated topography map is shown in Fig. 3 for the same domain. As thermodynamic and dynamic effects associated with convective and shallow clouds can be explicitly resolved at finer grid spacings, the Grell-Freitas cumulus scheme was turned off in D-4 and D-5 (Skamarock et al., 2008).

For the representation of the urban canopy physical processes and features, the Single-layer Urban Canopy Model (SLUCM) (Kusaka et al., 2001; Kusaka and Kimura, 2004), coupled to the Noah LSM (Chen and Dudhia, 2001), was used. The UHI simulations performed by Silva et al. (2021) for the Lisbon Metropolitan Area, using the same model configuration as this study, but forced by the ERA-Interim reanalysis from the European Centre for Medium-Range Weather Forecasts (ECMWF) (Dee et al., 2011), have shown that the SLUCM is less sensible to the number and distribution of vertical levels than the Building Effect Parameterization (BEP) multi-layer urban canopy

Table 1
Summary of the Lisbon UHI simulation experiments.

Simulation name	Simulation period/ () heatwave period	Urban LULC categories	Anthropogenic heat	Irrigation scheme
NURB_HIST	00 UTC of 17(18)/06/2000–00 UTC of 22/06/2000	No[1]	No	No
URB_HIST1	–	Yes (current Lisbon)	No	No
URB_HIST2	–	Yes (current Lisbon)	Yes	Yes
URB2050_HIST	–	Yes (Lisbon 2050)	Yes	Yes
URB2100_HIST	–	Yes (Lisbon 2100)	Yes	Yes
NURB_LONG	00 UTC of 09(10)/07/2098–00 UTC of 20/07/2098	No[1]	No	No
URB2100_LONG	–	Yes (Lisbon 2100)	Yes	Yes

[1] Urban LULC categories replaced by *cropland/woodland mosaic*.

model (Martilli et al., 2002).

Aiming to evaluate the ML's UHI during the HIST and LONG heatwaves, and to account for anthropogenic heat effects, irrigation of urban green spaces, and future urban consolidation, several WRF simulations forced by the MPI-ESM (LR) GCM were performed. The simulations and heatwave periods are described in Table 1, as well as the LULC, anthropogenic heat, and irrigation options used. All

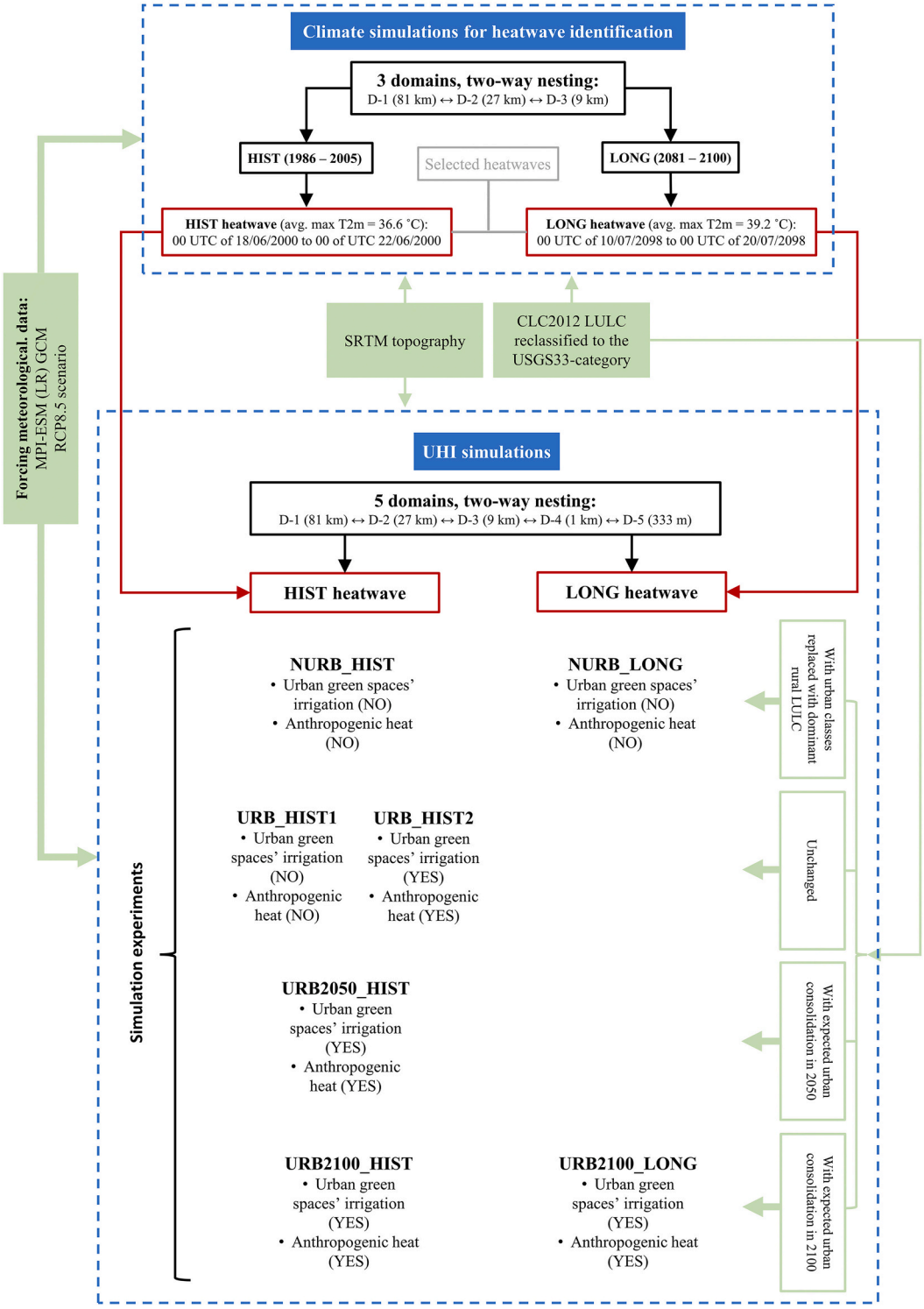

Fig. 4. Flow chart of the climatic and UHI simulations performed in this study.

the simulation periods described in Table 1 include a model spin-up of 24 h that is discarded from the analysis. The heatwave identified in HIST period allows the study of the city's growth relative impact, anthropogenic heat, and irrigation of the urban green fraction on the UHII. The heatwave of the LONG period is used to evaluate the relationship between heatwave and UHI intensities. In total, five simulations of the HIST period heatwave and two simulations of the LONG period heatwave were performed. Note that these simulation experiments do not consider possible demographic and traffic fluctuations, nor the possible advance or retreat of the water bodies surrounding the ML area that can occur in future climate scenarios.

For the assessment of the UHII and spatial patterns, the "local method" is used. This UHI identification method has been used in several studies (e.g., Georgescu et al., 2011; Ma et al., 2017; Silva et al., 2021) and is based on the temperature difference at each urban location when the model LULC is considered urban, and when it is replaced by the dominant rural LULC category of the urban surroundings. Hence, the application of the "local method" always requires two simulations, one considering the urban LULC and another including a hypothetical pre-urban LULC. As *cropland/woodland mosaic* is the most represented LULC class in domain D-5, covering 33.7% of the total area of the domain (excluding water), the model's urban LULC categories (i.e., *Low Intensity Residential* – LIR; *High Intensity Residential* – HIR; and *Industrial or Commercial* - IC) were replaced with this rural category. In this study, the simulations representing the pre-urban scenario of the HIST and LONG heatwaves are the NURB_HIST and NURB_LONG, respectively (see Table 1). It should be noted that the "local method" only accounts for urban canopy effects on the UHI, since local geographic effects are removed when using this UHI identification method. The preference for the "local method" instead of "classic method", that compares the urban temperature with the temperature of the urban surroundings, is related to the fact that this study is focused on the ML's area, where most of the LULC is composed by urban surfaces and where the future urban consolidation is considered. As in Silva et al. (2021), LIR, HIR, and IC, urban LULC classes have respectively 50%, 90%, and 95% of urban fraction, being the remainder fraction occupied with urban green spaces. Thermal and geometric parameters are also the same as in Silva et al. (2021).

Taking into consideration the simulation experiments described in Table 1, the following UHI fields and what they express are defined:

- UHI1_HIST (difference between urban points of URB_HIST1 and NURB_HIST simulations) – allows the study of the present impact of the ML's urban areas without considering the effects of anthropogenic heat and urban green spaces' irrigation;
- UHI2_HIST (difference between ML's urban grid points of URB_HIST2 and NURB_HIST simulations) – allows the evaluation of the collective impact of the anthropogenic heat and irrigation of urban green spaces;
- UHI3_HIST (difference between ML's urban grid points of URB2050_HIST and NURB_HIST simulations) – enables the study of the impact that the urban areas to consolidate by 2050 have on the ML's UHI intensity and distribution;
- UHI4_HIST (difference between ML's urban grid points of URB2100_HIST and NURB_HIST simulations) – enables the study of the impact that the urban areas to consolidate by 2100 have on the ML's UHI intensity and distribution;
- UHI_LONG (difference between ML's urban grid points of URB2100_LONG and NURB_LONG) – establishes the relationship between UHI and heatwave intensities, by comparing UHI_LONG with UHI4_HIST.

A flow chart of the methodology employed in the climatic and UHI simulations performed in this study is shown in Fig. 4.

2.2. Anthropogenic heat

The amount of anthropogenic heat release in cities is directly related to their population number. According to Sailor and Lu (2004), the magnitude of the anthropogenic heat, Q_f, can be divided into three components that represent its major sources of heat release in urban environments:

$$Q_f = Q_V + Q_B + Q_M \tag{1}$$

where the subscripts V, B, and M indicate vehicles, buildings, and human metabolism, respectively. The heat released by buildings can be further divided into heat directly rejected from electric energy consumption and heat released from the burning of fossil fuels used in heating during the cold season (can be ignored during summer periods).

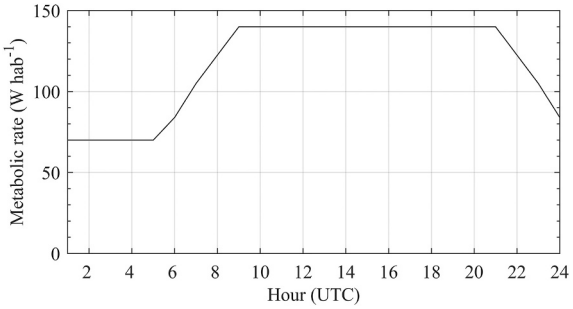

Fig. 5. Diurnal profile of the human metabolic rate (W hab^{-1}).

These anthropogenic heat components can be defined as a function of the population density, meaning that it is only necessary to compute their values per capita and multiply them by the population density.

2.2.1. Human metabolism

Typically, the heat resultant from human metabolism, Q_M, represents the smallest percentage of the total anthropogenic heat, and it is related with the level of physical activity during the day. According to Fanger (1970) and Hall (2015), during the day the metabolic rates for a 70 kg adult are 115 W hab^{-1} in rest and 230 W hab^{-1} walking, while at sleep the rates reduce to 70 W hab^{-1}. In this study, a diurnal mean value of 140 W hab^{-1} was considered. As in Sailor et al. (2016), a three hour transitional period was used during the morning and evening hours. Fig. 5 shows the diurnal profile of the heat resultant from human metabolism.

2.2.2. Buildings

The electric energy consumption due to home appliances, air conditioning, and lighting results in a variable percentage of energy wasted as heat, depending on the level of thermal insulation of the buildings, indoor temperature, and the location of the equipment (i.e., inside or outside the building).

According to Sailor et al. (2016), the electric energy consumption, E_{HR}, at any city can be given by $E_{HR} = E_{DPC}f(hour)$, where E_{DPC} is the daily energy consumption per capita and where

$$\sum_{1}^{24} f(hour) = 1.0 \tag{2}$$

For the summer $f(hour)$ is represented by the diurnal profile of Fig. 6, with minimum values at nighttime and maximum values during the daytime period.

2.2.3. Transport

Assuming that the distance per capita covered by vehicles has little seasonal variation, the hourly profile of the emissions from vehicles can be estimated using hourly data from traffic. Following Sailor et al. (2016), using the hourly traffic fraction profile, F_t, shown in Fig. 7, and the values of the distance per capita covered by vehicles, DVD, the heat released by the vehicles at a given hour of the day can be estimated through

$$Q_V(h) = DVD.F_t(h).\rho_{population}(h).EV \tag{3}$$

where $\rho_{population}(h)$ is the hourly population density, which is assumed to be constant in this study, and EV is the energy released *per* vehicle, per kilometer covered, and is given by

$$EV = \frac{NHC.\rho_{fuel}}{FE} \tag{4}$$

where NHC is the heat resulting from the combustion of gasoline or diesel (J kg^{-1}), ρ_{fuel} is the density of the fuel (kg l^{-1}) and FE is the mean fuel consumption (km l^{-1}).

The profile of Fig. 7 represents the average daily traffic profile of 61 cities of the United States of America, being the variation from city to city negligible. Hence, in this study, it is assumed that the daily traffic profile for the Lisbon Metropolitan Area has the same shape as the one from the USA cities.

2.3. Anthropogenic heat in the WRF single-layer urban canopy model

In the SLUCM model, there is the option for the inclusion of anthropogenic heat to each urban LULC class (i.e., LIR, HIR, and IC). For each one of these urban classes, a value corresponding to Q_{fmax} (in units of W m^{-2}) is multiplied by the nondimensional profile of Fig. 8.

For the population density in D-5, a constant value of $\rho_{pop} = 5064$ hab km^{-2} (PORDATA, 2018) was considered, as this corresponds

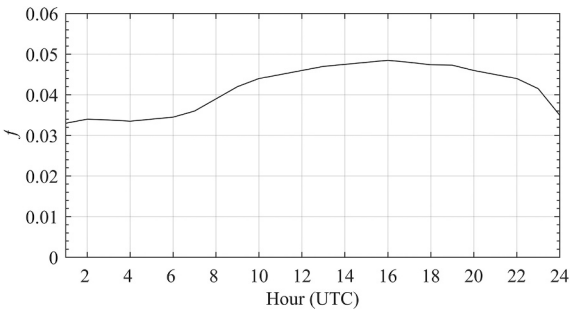

Fig. 6. Non-dimensional diurnal profile of the electric energy consumption.

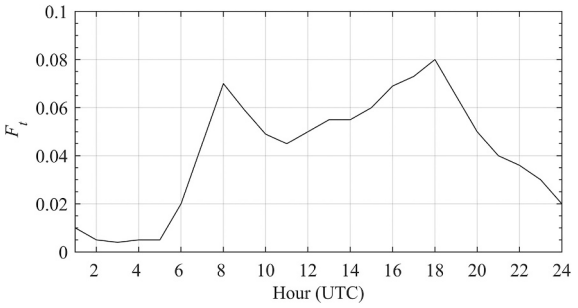

Fig. 7. Diurnal traffic profile.

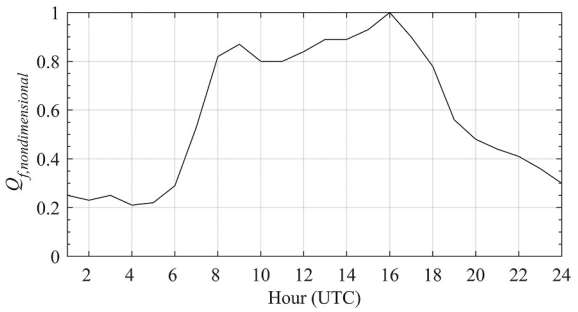

Fig. 8. Diurnal cycle of the nondimensional anthropogenic heat fraction.

to the population density of the ML, which is mostly covered by urban LULC. Since WRF computes anthropogenic heat fluxes only for urban grid cells, this was considered an adequate value for the whole D-5 domain. It is worth noting that diurnal variations in population density were not considered, and that population density is assumed constant across all urban LULC classes. For the application of the previous sections formulations and for obtaining the different components of the anthropogenic heat, it was considered that $FE = 16.6\ \text{km}\ \text{l}^{-1}$ (average value for EU-28 and equivalent to an average urban fuel consumption of ~6 *l* 100 km^{-1} for the year of 2017) (Diaz et al., 2020), $\rho_{\text{fuel}} = 0.85\ \text{kg}\ \text{l}^{-1}$ (assumed the same for both gasoline and diesel), $DVD = 10.3\ \text{km}\ \text{hab}^{-1}\text{dia}^{-1}$ (INE, 2018), $NHC = 45 \times 10^6\text{J}\ \text{kg}^{-1}$, and $E_{DPC} = 11.4767\ \text{kWh}\ \text{dia}^{-1}\ \text{hab}^{-1}$ (PORDATA, 2019).

Fig. 9 shows the diurnal cycle profiles for each one of the anthropogenic heat components described previously, as well as their total. A $Q_{fmax} = 6.2\ \text{W}\ \text{m}^{-2}$ was used for each LULC class and then multiplied by the non-dimensional profile of Fig. 8 to obtain the diurnal cycle of the total anthropogenic heat, which was used within the URBPARM.TBL of the WRF model.

2.4. Urban green spaces' irrigation

The irrigation of urban green spaces is a common practice during summer. Besides its contribution to the maintenance of the urban green spaces, irrigation contributes to the increase in evaporative cooling near the surface and, hence, for greater energy efficiency of the surrounding buildings (Yang and Wang, 2015). Urban canopy models frequently overestimate the surface sensible heat fluxes and underestimate the latent heat fluxes (Huang et al., 2019; Shiguang and Fei, 2014), which could potentially result in greater vertical

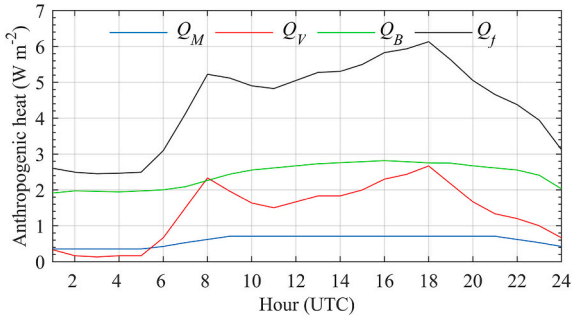

Fig. 9. Diurnal profiles of the total anthropogenic heat (black) and its components: human metabolism (blue), vehicles (red), and buildings (green). Units: $W\ m^{-2}$.

instability and surface temperature. The use of irrigation schemes in urban canopy models allows for a better representation of these processes and, consequently, a better evaluation of UHIs (Shiguang and Fei, 2014).

The SLUCM model includes an irrigation scheme activation option for simulating the irrigation of urban green spaces for the months between May and September, every day, between 2100 and 2200 local time (Yang et al., 2015). The irrigation effect is reproduced by increasing the volumetric soil moisture content in the first top two soil layers (first 0.4 m of soil, which represent the vegetation root zone) to a value of 0.329 m^3m^{-3} (i.e., the threshold reference value below which vegetation begins to stress due to decreased transpiration). Hence, water uptake by vegetation roots is not limited by soil moisture availability.

In this study the urban green spaces irrigation option was considered in URB_HIST2, URB2050_HIST, URB2100_HIST, and URB2100_LONG simulation experiments (see Table 1) by activating the IRI_SCHEME option in the URBPARM.TBL of the WRF model.

2.5. Surface energy balance

In the Noah LSM/SLUCM system, embedded in the WRF model, surface heat fluxes are estimated through the urban fraction parameter (F). For a specific model grid cell, heat fluxes from vegetated surfaces are computed by the Noah LSM, while the SLUCM computes the fluxes over artificial surfaces (Chen et al., 2011; Kusaka and Kimura, 2004). In this modelling system, the vegetated fraction of the LIR, HIR, and IC LULC is classified as "NATURAL" LULC, which assumes the same physical parameters of the *cropland/grassland mosaic* class (see Table S1 of Silva et al., 2021 for details about the physical parameters of the different LULC classes).

In this study, the representation of the surface energy balance (BAL) when considering anthropogenic heat in the Noah LSM/SLUCM system is given by

$$BAL = SH + LH - GRD \tag{5}$$

with

$$BAL = R_n + Q_f \tag{6}$$

where R_n is the net radiation, Q_f is the anthropogenic heat flux, SH, LH and GRD, represent the sensible, latent, and ground surface heat fluxes, respectively. Particularly, within a model grid cell classified as LIR, HIR, or IC, the SH flux is computed as,

$$SH = SH_{urb} \times F_{urb} + SH_{veg} \times F_{veg} \tag{7}$$

where F_{veg} and F_{urb} represent each model's grid cell vegetated and urban fractions, respectively. The same equation can be applied to the LH and GRD fluxes.

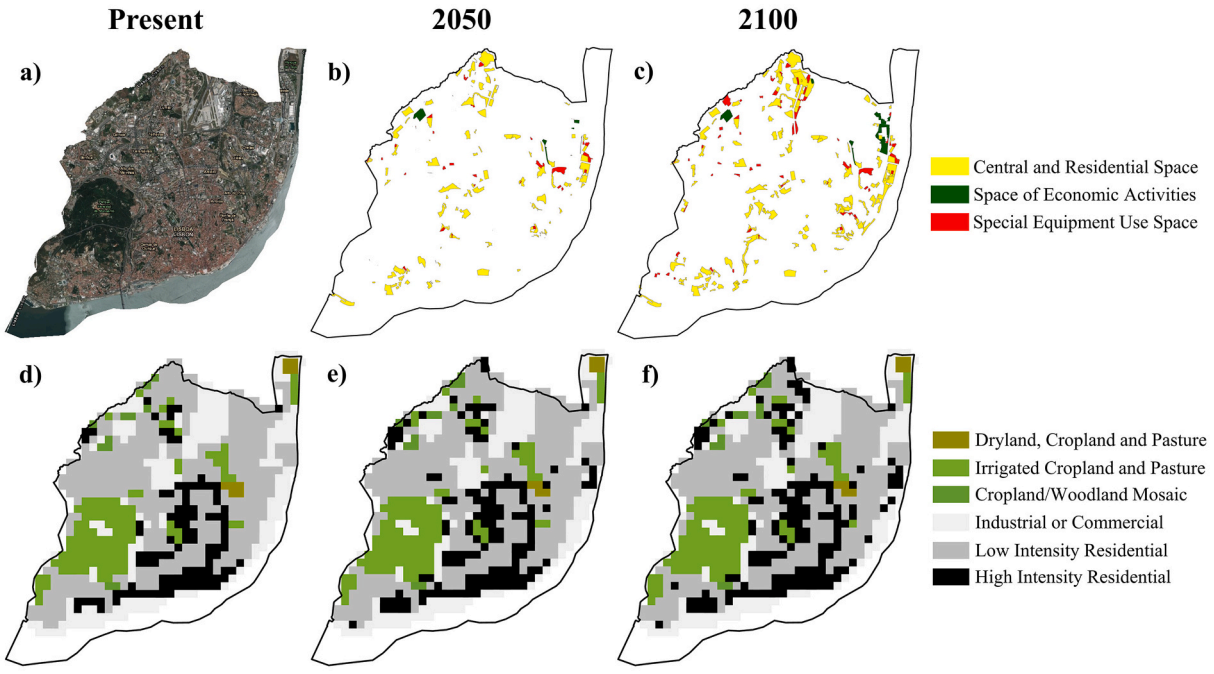

Fig. 10. a) ML orthophoto in the present (2012 LULC); b) and c) ML urban areas to consolidate by 2050 and 2100, respectively; d) representation of WRF land use map in the present, e) including the urban areas to consolidate by 2050, f) and including the urban areas to consolidate by 2100. The white areas within the ML limits of Fig. 10d), e), and f) correspond to the public water domain.

2.6. Future consolidation of the municipality of Lisbon urban areas

For the inclusion of future urban changes in WRF's LULC, the urban areas to consolidate by 2050 and 2100 were provided by the Lisbon City Council. The first step was to project the supplied shapefiles to the standard coordinate system of WRF (i.e., World Geodetic System 1984), followed by the conversion of the projected shapefiles into ascii format with pixel area equal to the CLC2012. The resultant ascii files, corresponding to the urban areas to consolidate by 2050 and 2010, and classified as *central and residential space*, were reclassified to HIR, while pixels previously classified as *space of economic activities* and as *special equipment use space* were both reclassified to IC.

After the reclassification of the urban areas to consolidate in the ascii files, they were overlaid with the original CLC2012 ascii file. The pixels of the original CLC2012 ascii file coincident with the areas to consolidate were reclassified to the new categories. Hence, two distinct files were created: the first one includes the areas to consolidate by 2050 and the second one includes the areas to consolidate by 2100. The resultant ascii files were then converted into binary format to be assimilated and interpolated by WRF preprocessing system (WPS). Fig. 10a) shows the 2012 orthophoto of the ML; b) and c) shows the shapefiles representation of the areas to consolidate in ML by 2050 and 2100, respectively; d), e), and f) shows the WRF's LULC in ML without the areas to consolidate (Present LULC), with the areas to consolidate by 2050, and with the areas to consolidate by 2100, respectively. Here, the "Present" LULC represents the CLC2012 LULC. Complementarily to Fig. 10, in Table 2, is shown the number of grid points/percentage of each urban LULC in the ML for the present, 2050, and 2100; and in Table 3 is shown the statistics of the transition between LULC classes in number of grid points/percentage for 2050/2100/2100 relative to Present/2050/Present, respectively. It is evident that, compared with the present LULC map, the ML is expected to densify through the conversion of LIR (with 50% urban fraction) areas into HIR (with 90% urban fraction); there is a decrease of about 10.3% (5.9%) in LIR class, an increase of 45.2% (30.8%) in HIR class, and a decrease in IC of 4.3% (4.8%) grid points by 2100 (by 2050).

3. Results

3.1. Impact of anthropogenic heat, urban green spaces' irrigation, and urban areas to consolidate on the UHI

In this section, the impacts that the anthropogenic heat, irrigation of urban green spaces, and the inclusion of urban areas to consolidate by 2050 and 2100 have on the modeled UHI are addressed for the ML. These impacts are considered, separately or together, using the different HIST heatwave simulations results.

Fig. 11 shows the heatwave averaged mean diurnal cycle of the two-meter temperature (T2m) over ML's urban grid points from the HIST heatwave simulations. As expected, the lowest T2m values are produced by the NURB_HIST simulation for the entirety of the diurnal cycle, as urban LULC classes were replaced by *cropland/woodland mosaic*. In contrast, the URB2100_HIST produces the highest T2m, especially during nighttime, as it includes all of the effects considered in this study.

As previously mentioned, the evaluation of the UHI during the HIST heatwave is done with respect to the reference simulation of the same period (i.e., NURB_HIST simulation). Therefore, Fig. 12 shows the diurnal cycle of the heatwave averaged UHIs defined in Section 2.1.2. Complementarily, a summary of the mean statistics decomposition of these UHIs into the different urban LULC categories is presented in Table 4. For this particular heatwave the near-surface UHI is positive in all simulations, with average daytime values ranging from 0.48 °C in UHI3_HIST and 0.6 °C in UHI4_HIST, while nighttime values range from 1.27 °C in UHI2_HIST and 1.75 °C in UHI4_HIST. Among the different factors that differentiate the HIST heatwave simulations, the consolidation of the future urban areas is the one that has the most impact in the increase of the UHII, particularly when the areas to consolidate by 2100 are considered. The UHI4_HIST reaches a nighttime maximum intensity of 2.34 °C during the heatwave period over the ML (not shown), and the nighttime UHII decreases when comparing UHI1_HIST and UHI2_HIST. This reduction may be related with the inclusion of irrigation in the urban green spaces, which introduces moisture in the first layers of soil and reduces its temperature. As can be seen, the effect introduced by the urban green spaces' irrigation offsets the warming effect of the anthropogenic heat release during the nighttime period in all urban LULC classes. Another aspect to be highlighted is the lower daytime intensity of the UHI3_HIST compared with UHI2_HIST, which is verified in all urban classes. This indicates that the changes introduced in the model's LULC map due to the areas to consolidate by 2050 did not contribute for the increase in the daytime temperature. However, this is mostly owed to a reduction of about 4.3% and 5.9% in the IC and LIR areas, respectively, together with the increase in the HIR areas by 30.8% that leads

Table 2
Number of grid points / % of each LULC class within the ML area for the Present (2012), 2050, and 2100 LULC, over the domain D-5 grid. The acronyms represent: LULC – land use land cover; DEP – dryland cropland and pasture; ICP – irrigated cropland and pasture; CWP – cropland/woodland mosaic; LIR – low intensity residential; HIR – high Intensity Residential; IC – industrial or commercial.

LULC class	Present (2012)	2050	2100
DCP	9 / 1.1%	8 / 1.0%	8 / 1.0%
ICP	114 / 14.0%	114 / 14.0%	114 / 14.0%
CWM	11 / 1.4%	12 / 1.5%	13 / 1.6%
LIR	390 / 47.9%	367 / 45.1%	350 / 43.0%
HIR	104 / 12.8%	136 / 16.7%	151 / 18.6%
IC	186 / 22.9%	177 / 21.7%	178 / 21.9%

Table 3
Transition between LULC classes within the ML area for 2050 / 2100 / 2100 relative to Present / 2050 / Present, respectively, over the domain D-5 grid. The acronyms represent: LULC – land use land cover; DEP – dryland cropland and pasture; ICP – irrigated cropland and pasture; CWP – cropland/ woodland mosaic; LIR – low intensity residential; HIR – high Intensity Residential; IC – industrial or commercial.

Present (2012) LULC	2050 LULC (grid points / %)					
	DCP	ICP	CWM	LIR	HIR	IC
DCP	-1 / -11.1%	–	–	–	1 / 1.0%	–
ICP	–	-2 / -1.8%	–	1 / 0.3%	1 / 1.0%	–
CWM	–	–	–	–	–	–
LIR	–	2 / 1.8%	1 / 9.1%	−24 / -6.2%	21 / 20.1%	–
HIR	–	–	–	–	–	–
IC	–	–	–	–	9 / 8.7%	−9 / -4.8%
Total	−1 / -11.1%	0 / 0.0%	1 / 9.1%	−23 / -5.9%	32 / 30.8%	−9 / -4.8%
2050 LULC	2100 LULC (grid points / %)					
	DCP	ICP	CWM	LIR	HIR	IC
DCP	–	–	–	–	–	–
ICP	–	−2 / -1.8%	–	–	1 / 0.7%	1 / 0.6%
CWM	–	–	–	–	–	–
LIR	–	2 / 1.8%	1 / 8.3%	−17 / -4.6%	12 / 8.8%	2 / 1.1%
HIR	–	–	–	–	−1 / -0.7%	1 / 0.6%
IC	–	–	–	–	3 / 2.2%	−3 / -1.7%
Total	–	0 / 0.0%	1 / 8.3%	−17 / -4.6%	15 / 11.0%	1 / 0.6%
Present (2012) LULC	2100 LULC (grid points / %)					
	DCP	ICP	CWM	LIR	HIR	IC
DCP	−1 / -11.1%	–	–	–	1 / 1.0%	–
ICP	–	−4 / -3.5%	–	–	3 / 2.9%	1 / 0.5%
CWM	–	–	–	–	–	–
LIR	–	4 / 3.5%	2 / 18.2%	−40 / -10.3%	31 / 29.8%	3 / 1.6%
HIR	–	–	–	–	–	–
IC	–	–	–	–	12 / 11.5%	−12 / -6.5%
Total	−1 / -11.1%	0 / 0.0%	2 / 18.2%	−40 / -10.3%	47 / 45.2%	−8 / -4.3%

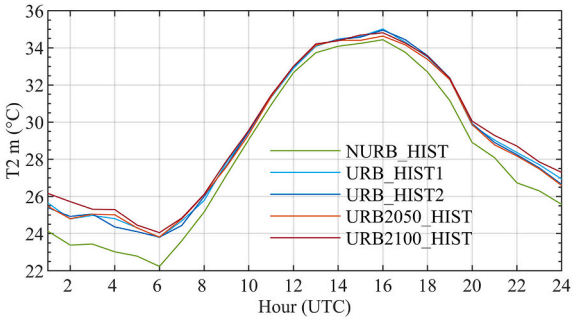

Fig. 11. Heatwave averaged mean diurnal cycle of the T2m over ML's urban grid points for the different simulation experiments of the HIST heatwave.

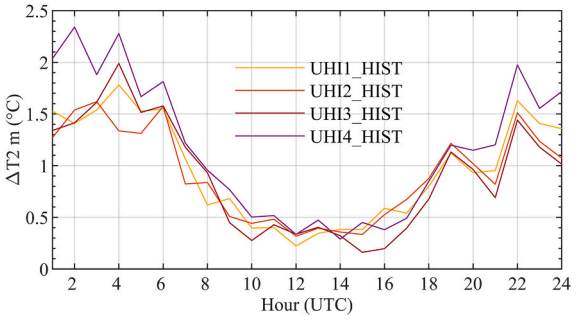

Fig. 12. Heatwave averaged mean diurnal cycle of the near-surface UHIs defined in Section 2.1.2 for the HIST heatwave.

Table 4
Daytime and nighttime mean statistics of the decomposition of the different UHIs from the HIST heatwave into the LIR, HIR, IC, and ALL urban LULC classes. Units: °C.

	Daytime mean				Nighttime mean			
UHI name	ALL	LIR	HIR	IC	ALL	LIR	HIR	IC
UHI1_HIST	0.54	0.54	0.68	0.49	1.41	0.47	2.64	2.53
UHI2_HIST	0.58	0.58	0.72	0.54	1.27	0.35	2.47	2.38
UHI3_HIST	0.48	0.46	0.60	0.47	1.35	0.27	2.49	2.48
UHI4_HIST	0.60	0.58	0.71	0.56	1.75	0.49	3.00	2.89

to higher shadowing effect. During nighttime there is a significant increase in the UHI3_HIST compared with UHI2_HIST, with the exception of the LIR class. The HIR and IC urban classes contribute the most for the total UHI during nighttime, with intensities reaching >2.5 °C in both classes, while the LIR class has an intensity more than five times smaller. During daytime the differences between the UHIs are smaller, with HIR areas having the highest intensities ranging between 0.6 °C and 0.72 °C. Minimum UHII is reached at 08 UTC in all urban classes. Interestingly, while near-surface UHII values remain almost constant during daytime, they increase at the surface, with this increase being inversely proportional to the increase in urban green fraction of each urban class (not shown).

Fig. 13 shows the heatwave averaged UHI1_HIST, UHI2_HIST, UHI3_HIST, and UHI4_HIST daytime and nighttime fields, with the corresponding heatwave averaged 10-m wind speed and direction. Consistent with the previous results, the UHII is much higher during nighttime than daytime, with UHI4_HIST showing the highest values. The differences between the UHIs are less visible during daytime, with all the UHIs showing approximately the same intensity. The nighttime UHI fields show greater contrast between the different urban classes, with the average UHII in the ML reaching 4.5 °C and an absolute maximum of 10 °C during the heatwave period in some locations of HIR and IC areas (not shown). Regarding the modeled wind speed and direction, the fields of Fig. 13 show an average daytime wind speed of approximately 2 m s^{-1}, predominantly from southeast direction, which contributes to the decrease of the UHII through advective cooling and turbulent heat fluxes. During nighttime, the wind speed decreases and the UHII increases, with the wind being mostly from the northeast direction.

Fig. 14 shows the differences between the UHI fields of Fig. 13, allowing for the assessment of the relative impact of the different changes introduced in the ML's UHI due to anthropogenic heat, urban green spaces' irrigation, and urban areas to consolidate by 2050 and 2100. The columns of the figure represent, respectively, the changes in daytime and nighttime T2m due to the combination of anthropogenic heat and urban green spaces' irrigation (UHI2_HIST – UHI_HIST), urban areas to consolidate by 2050 (UHI3_HIST – UHI2_HIST), and urban areas to consolidate by 2100 (UHI4_HIST – UHI2_HIST). The change in ML's average T2m during the diurnal

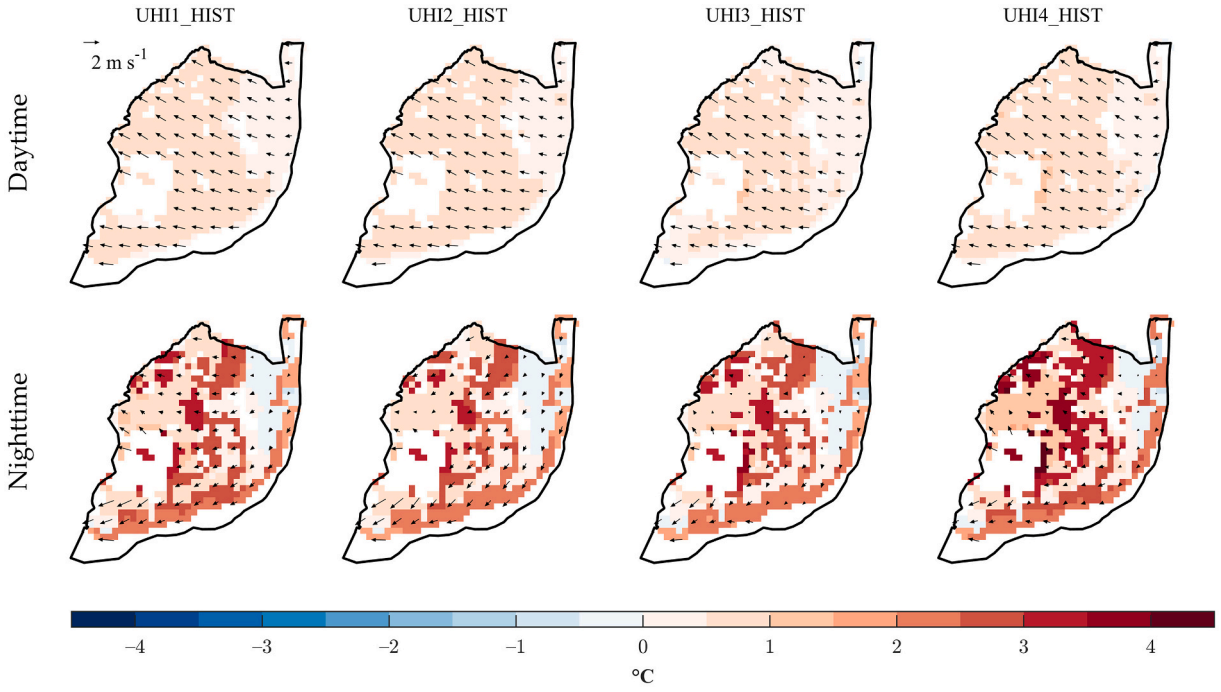

Fig. 13. Heatwave averaged daytime and nighttime UHI1_HIST, UHI2_HIST, UHI3_HIST, and UHI4_HIST fields. Vectors indicate heatwave averaged daytime and nighttime 10-m wind speed and direction (m s^{-1}).

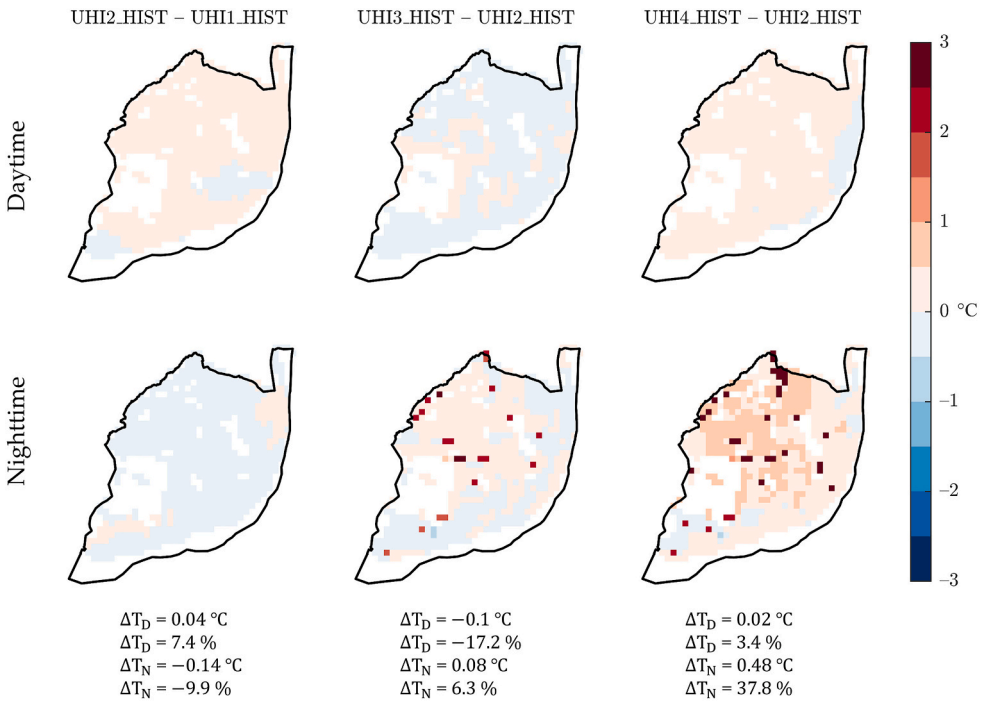

Fig. 14. Heatwave averaged daytime and nighttime differences between UHI2_HIST and UHI1_HIST (first column), UHI3_HIST and UHI2_HIST (second column), and UHI4_HIST and UHI2_HIST (third column). The ML average temperature difference for diurnal (ΔT_D) and nighttime (ΔT_N) periods is indicated below each column as absolute and percentual values.

(ΔT_D) and nighttime (ΔT_N) periods is indicated below each column of the figure as absolute and percentage values. The combined effect of anthropogenic heat and irrigation of urban green spaces leads to a reduction of 0.14 °C (−9.9%) in the nighttime UHII and to the increase of the daytime values by 0.04 °C (7.4%). The introduction of the urban areas to consolidate by 2050 leads to a decrease of 0.1 °C (−17.2%) in the daytime UHII and to an increase of 0.08 °C (6.3%) in the nighttime UHII. The decrease by 17.2% in the daytime UHI may be owed to the increase by 30.8% in HIR areas, and consequent increase in the shadowing effect and near-surface turbulent fluxes. Lastly, the urban areas to consolidate by 2100 led to an increase of 0.02 °C (3.4%) in the daytime UHII and 0.48 °C (37.8%) during nighttime compared with the values for the UHI2_HIST. Hence, the inclusion of the urban areas to consolidate by 2100 in model LULC contributes the most to the increase in the UHII during nighttime. Despite this, it should be noted that the introduction of the areas to consolidate by 2050 (i.e., UHI3_HIST – UHI2_HIST) and 2100 (i.e., UHI4_HIST – UHI2_HIST) may have a small impact in the contribution of anthropogenic heat and irrigation effects to the UHII, owed to the fact that the urban fraction marginally changes in the ML through the inclusion of the new urban LULC areas.

As changes in the physical and dynamical properties of the underlying urban LULC modulate the surface and near-surface UHII and distribution, Table 5 displays the daytime and nighttime mean statistics of the surface fluxes of SH, LH, GRD, and their balance (BAL) averaged over ML's urban grid points, for all the simulation experiments of the HIST heatwave. Daytime upward SH and absolute downward GRD fluxes increase from NURB_HIST to URB2100_HIST, with the exception of URB2050_HIST where these fluxes suffer a slight reduction when compared with URB_HIST2 simulation. This is reflected through a reduction in daytime UHI of 0.1 °C shown in Table 4, and it is mainly caused by the decrease in LIR and IC urban classes areal coverage (see Table 2 and Table 3). In contrast, the daytime LH fluxes decrease, except for URB_HIST2 relative to URB_HIST1 simulation. The slight increase in URB_HIST2 LH fluxes is possibly owed to the inclusion of urban green spaces' irrigation that contributes for a slight increase in these fluxes during early

Table 5
Summary of the daytime and nighttime mean statistics of the surface fluxes of sensible heat (SH), latent heat (LH), ground heat (GRD), and the surface energy balance (BAL), averaged over urban grid points. Units: W m^{-2}.

	Daytime mean				Nighttime mean			
Simulation experiment	SH	LH	GRD	BAL	SH	LH	GRD	BAL
NURB_HIST	84.5	251.3	−91.5	427.3	−16.7	19.5	46.0	−43.2
URB_HIST1	138.1	131.9	−118.4	388.4	5.1	5.1	77.2	−67.0
URB_HIST2	143.6	132.3	−121.1	397.0	6.7	4.9	79.0	−67.4
URB2050_HIST	143.3	123.7	−120.3	387.3	7.3	4.8	78.7	−66.6
URB2100_HIST	147.9	120.6	−122.6	391.1	6.7	4.5	79.6	−68.4

morning in HIR classes, as we will see in Fig. 16. As expected, nighttime upward SH and LH fluxes are much lower in magnitude than the daytime ones, with upward GRD fluxes representing the larger fraction of the total nighttime energy fluxes. Upward GRD fluxes are positive during nighttime and increase as changes are introduced in the different simulations, excluding the URB2050_HIST simulation, that shows a decrease in the upward GRD flux in comparison with URB_HIST2 simulation. Again, this is mostly owed to the reduction in LIR and IC urban classes' areal coverage, and a consequence of the decrease in the daytime downward GRD fluxes of URB2050_HIST relative to URB_HIST2.

To help with the interpretation of the previous results, Fig. 15 shows the heatwave averaged diurnal cycle of the differences between the surface heat fluxes of URB_HIST2 relative to URB_HIST1, URB2050_HIST relative to URB_HIST2, and URB2100_HIST relative to URB_HIST2 simulations. As in Table 5, the fluxes represent averages over ML's urban grid points. All SH fluxes differences have positive sign during most of the daytime and nighttime, with the exception of the difference between URB2050_HIST and URB_HIST2 in the early morning, when differences have negative sign. Nevertheless, the inclusion of the urban areas to consolidate in ML by 2050 led to an increase in the upward SH fluxes during the nighttime. Regarding the LH fluxes, there is a slight daytime increase of 0.4 W m^{-2} due to the effect of urban green spaces' irrigation. However, significant reductions in the daytime LH release are obtained by including the urban areas to consolidate by 2050 (-8.6 W m^{-2}) and 2100 (-11.7 W m^{-2}) in the LULC, compared with URB_HIST2 simulation. This is mostly owed to the increase in HIR and to the reduction of LIR areal coverage within the ML, that results in the loss of urban green spaces. Changes in downward GRD fluxes are less obvious, but there is an overall daytime increase in URB_HIST and URB2100_HIST simulations. Similar results are found for the nighttime upward GRD fluxes. Lastly, nighttime upward BAL fluxes slightly increase by accounting for anthropogenic heat and urban green spaces' irrigation when compared to the simulation without anthropogenic heating and irrigation, slightly decrease when considering the urban areas to consolidate by 2050, and increase with the introduction of the urban areas to consolidate by 2100.

The effects of the changes introduced in the different simulation experiments become clearer when looking at the decomposition of the total fluxes into the different urban LULC classes (i.e., LIR, HIR, and IC), as shown in Fig. 16. It is noteworthy that the different profiles in Fig. 16 are weighted by the number of grid points of each urban class, relative to the total number of urban grid points in each simulation.

Changes in surface fluxes due to anthropogenic heat and irrigation are small (blue dashed lines) in all urban classes, except during early morning. Larger changes are found in the SH and GRD fluxes of HIR class, mainly due to the introduction of the areas to consolidate by 2050 and 2100 (red and black solid lines, respectively). For the HIR class, there is an increase in SH fluxes (up to 20 W m^{-2}) and an increase by the same amount in the downward GRD fluxes during daytime. LH fluxes also suffer a small increase in HIR areas, but this is at the expense of the loss in LIR areal coverage due to the changes introduced by the urban areas to consolidate by 2050 and 2100. During nighttime, there is an increase in the upward GRD flux (up to 10 W m^{-2}) due to the increase in the areal coverage of HIR areas that contributes to the increase in nighttime UHII. As a consequence of the reduction in LIR areal coverage, there is a decrease in SH and LH fluxes in LIR class during daytime. Changes due to the IC class are much smaller, as these classes have smaller changes relatively to the contemporary land use. The surface fluxes in LIR class contrast with the ones from HIR but are most evident in the LH and SH fluxes due to the reduction in the representation of urban green spaces in the ML.

3.2. *UHI during long-term future heatwave and comparison with other heatwaves*

Fig. 17 shows the heatwave averaged diurnal cycle of the T2m averaged over urban grid points' locations for the URB2100_LONG and NURB_LONG simulations described in Table 1. As said before, the LONG heatwave refers to the heatwave with the highest average maximum temperature of the long-term future climatic simulations. For the ML's area, and by considering the presence of urban LULC classes, the average maximum temperature during the heatwaves reaches 37.89 °C and 37.74 °C at 16 UTC in the URB2100_LONG and NURB_LONG simulations, respectively, with small differences between the modeled daytime T2m between both simulations. During nighttime, URB2100_LONG minimum T2m is 28.15 °C, while in NURB_LONG is 26.87 °C, both at 06 UTC.

The UHI_LONG diurnal profile is shown in Fig. 18, together with the diurnal profiles of the UHI4_HIST and the August 2003 heatwave event UHI (i.e., UHI_2003) studied by Silva et al. (2021), all over the ML. Notice that the comparison between the UHI_2003 with the UHI_LONG and UHI4_HIST is limited by the fact that UHI_2003 does not consider the effects of anthropogenic heat, urban green spaces' irrigation, or urban LULC future consolidation. Although these effects could lead to a significant increase in the UHI_2003 intensity, as can be seen by comparing the UHI1_HIST and UHI4_HIST diurnal profiles in Fig. 12, they do not affect the comparative analysis between the UHIs of Fig. 18, especially during daytime. Complementarily to Fig. 18, a summary of the daytime and nighttime mean statistics of these UHIs is shown in Table 6. The UHI_LONG nighttime intensity is 1.07 °C but can reach on average 2.3 °C in HIR and IC areas, while daytime values reach a maximum 0.37 °C in HIR areas. Despite the higher heatwave intensity (39.22 °C) and associated heatwave duration (10 days), the UHI_LONG has weaker daytime and nighttime intensity than the UHI4_HIST. In fact, as the UHI_2003, an urban cold island of -0.28 °C is obtained in LIR areas in UHI_LONG during nighttime. As can be seen, the UHI_2003 is the only one with negative signal during the daytime in all urban classes (see Table 6), even though its mean maximum temperature is the second highest from the three heatwaves shown in Fig. 18 (38.86 °C). From all the UHIs, the UHI4_HIST, associated with the heatwave with the weakest intensity (36.9 °C), is the one with highest daytime and nighttime intensity. Therefore a direct connection between heatwave intensity and UHII cannot be established without considering other influencing factors such as wind intensity and direction, since urban canopy effects are the same between the UHIs, excluding the UHI_2003.

The heatwave averaged nighttime and daytime UHI fields of the UHI_LONG, UHI4_HIST and UHI_2003 are shown in Fig. 19, together with the associated 10-m wind speed and direction vectors. Clearly, the UHII is controlled by the wind speed and direction, with UHIs under predominant northern wind conditions having much weaker and sometimes negative signal, while UHIs under

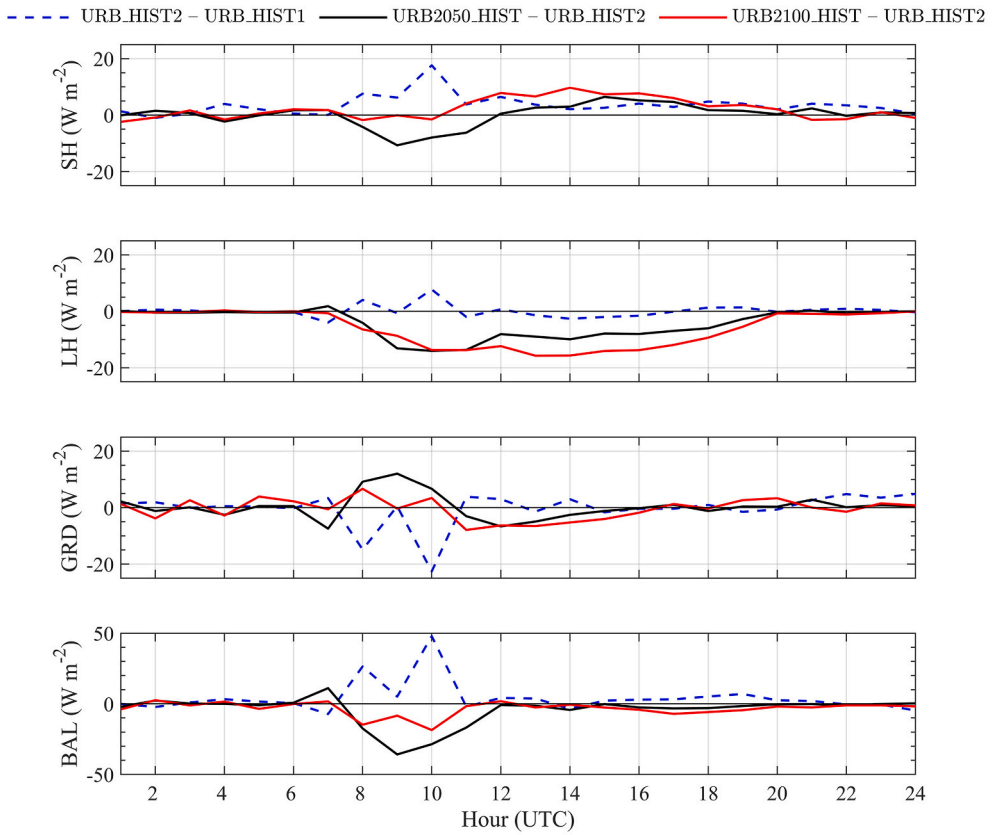

Fig. 15. Heatwave averaged diurnal cycle of the differences between URB_HIST2 and URB_HIST1, URB2050_HIST and URB_HIST2, and URB2100_HIST and URB_HIST2 surface fluxes of sensible heat (SH), latent heat (LH), ground (GRD), and the surface energy balance (BAL). Curves represent averaged values over urban grid points.

predominant southeasterly/southwesterly wind have stronger positive signal during nighttime and daytime periods. Additionally, LIR areas (with lower building heights and smaller urban fraction) with south-north orientation act as urban corridors, favoring urban canopy ventilation under northern wind conditions, as it is apparent in the UHI_LONG during nighttime, and UHI_2003 during daytime and nighttime periods.

4. Conclusions

In this study, the impacts that anthropogenic heat, urban green spaces' irrigation, and consolidation of urban LULC areas (up to 2050 and 2100) have on the ML's UHI were investigated using a coupled WRF-SLUCM modelling framework. These effects were assessed for a typical heatwave of the HIST period (1986–2005) and for the heatwave with highest average maximum temperature of the LONG period (2081–2100), both identified in climatic simulations forced by the GCM MPI-ESM (LR) output regarding the historical and RCP8.5 future climate scenario simulations. Therefore, synergies between UHII and heatwave intensity were also explored.

The results reveal that the anthropogenic heat influence on the ML's UHI is quite small, as these heat fluxes represent a slight change in the total urban SH fluxes compared with the amount of SH release due to urbanization. The combined effect of urban green spaces' irrigation and anthropogenic heat leads to an increase in the daytime UHI of 0.04 °C and a reduction in nighttime UHI of 0.14 °C, mostly due to the increase of soil moisture and consequent decrease in soil temperature.

Nighttime UHII in HIR and IC classes can be more than five times stronger than in LIR class, while daytime UHI is mostly uniform regarding its distribution and intensity across all urban classes. The most evident changes in the UHII were found during nighttime in HIR and LIR, due to the consolidation of urban areas by 2050 and especially by 2100, although an increase in the daytime UHII was also found by including the urban areas to consolidate by 2100. The decomposition of the surface heat fluxes into the different urban LULC classes shows a significant increase in daytime SH fluxes and downward GRD fluxes in HIR areas, owing to the increase in areal coverage of this LULC class by 2050 and 2100. During nighttime, the consolidation of the urban areas up to 2100 led to an increase of 37.8% in the UHII, mostly associated with the increase in nighttime upward GRD fluxes. By including the urban areas to consolidate by 2100, the UHII can reach >10 °C over large urban areas. Given that the methodology for the identification of the UHI used here (i.e., local method) only accounts for urban canopy effects and, as demonstrated by a previous study (Silva et al., 2021), the ML's geographic effects play an important role in its UHII and distribution, the UHII could be even greater if local geographic effects were considered.

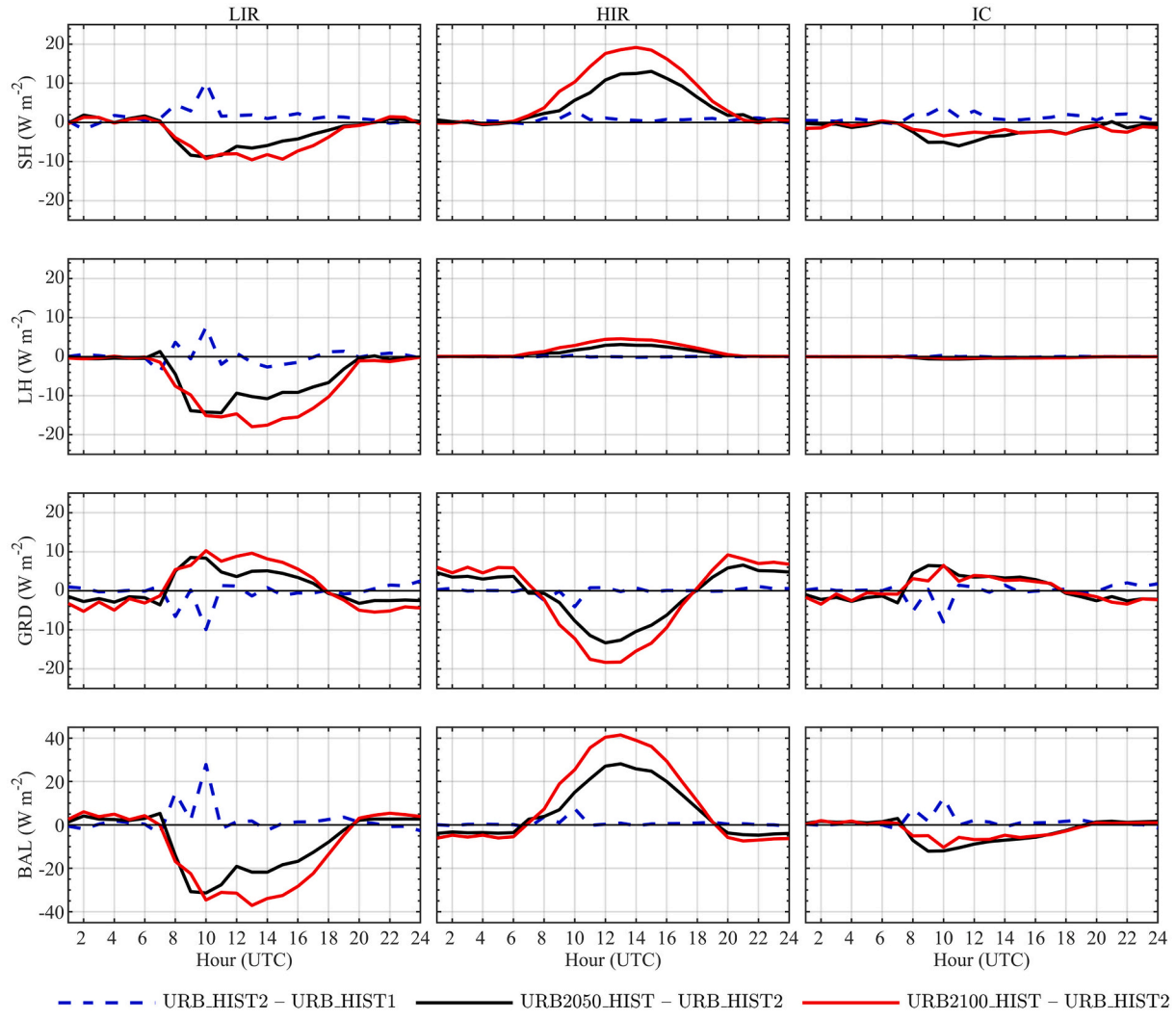

Fig. 16. Heatwave averaged diurnal cycle of the differences between URB_HIST2 and URB_HIST1, URB2050_HIST and URB_HIST2, and URB2100_HIST and URB_HIST2 surface fluxes of sensible heat (SH), latent heat (LH), ground (GRD), and the surface energy balance (BAL), for the different urban land use classes. The fluxes are weighted by the number of grid points of each urban class, relative to the total number of urban grid points in each simulation.

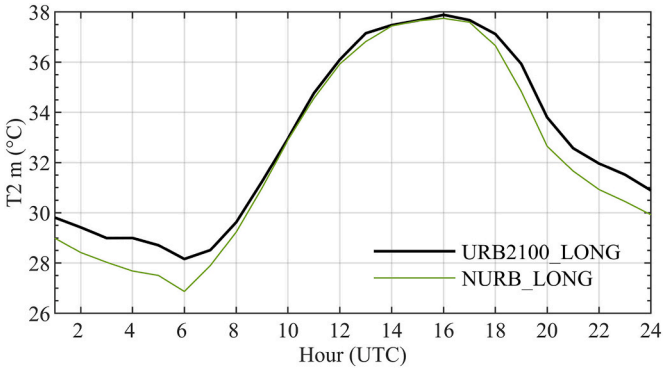

Fig. 17. Heatwave averaged diurnal cycle of the T2m over ML's urban grid points for the URB2100_LONG and NURB_LONG simulation experiments.

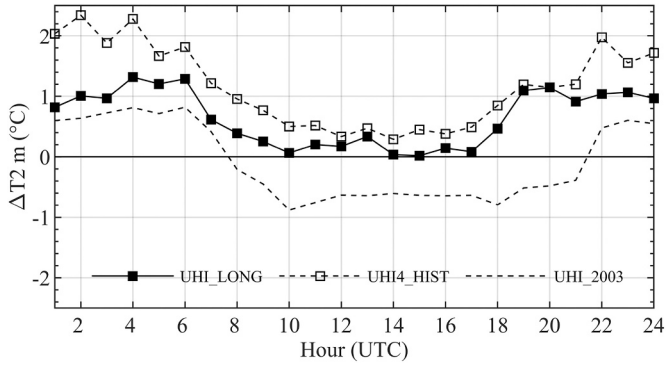

Fig. 18. Heatwave averaged diurnal cycle of the UHI_LONG, UHI4_HIST, and UHI_2003 over ML's area.

Table 6
Daytime and nighttime mean statistics of the decomposition of the UHI_LONG, UHI4_HIST, and UHI_2003 into the LIR, HIR, IC, and ALL urban LULC classes. Units: °C.

	Daytime mean				Nighttime mean			
UHI name	ALL	LIR	HIR	IC	ALL	LIR	HIR	IC
UHI_LONG	0.27	0.21	0.37	0.30	1.07	−0.28	2.33	2.32
UHI4_HIST	0.60	0.58	0.71	0.56	1.75	0.49	3.00	2.89
UHI_2003*	−0.69	−0.80	−0.63	−0.64	0.62	−0.09	1.47	1.43

* UHI values for the August 2003 heatwave event does not consider the effects of anthropogenic heat, urban green spaces irrigation, or urban LULC future consolidation.

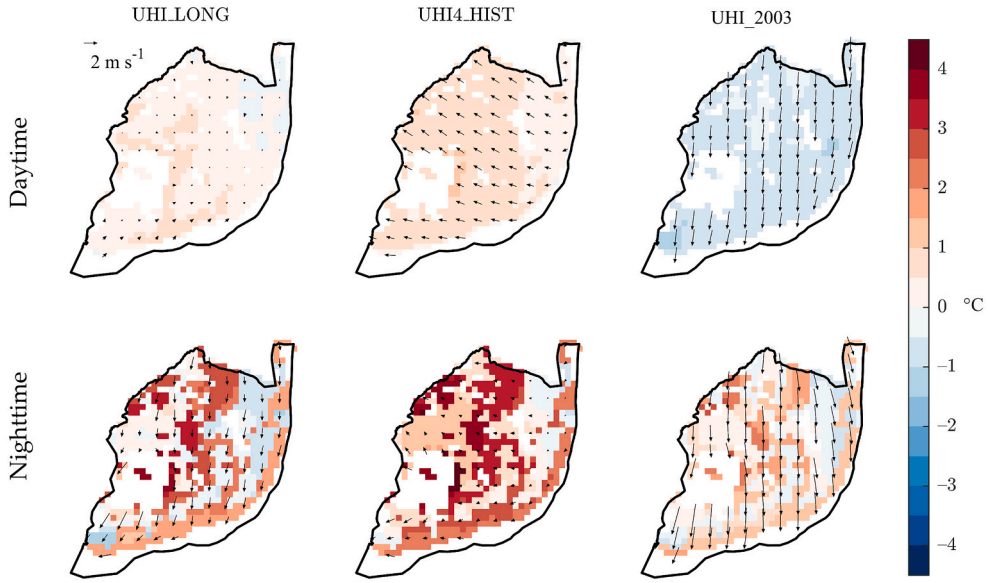

Fig. 19. Heatwave averaged daytime and nighttime UHI_LONG, UHI4_HIST, and UHI_2003 fields. Vectors indicate heatwave averaged daytime and nighttime 10-m wind speed and direction (m s^{-1}).

Lastly, the analysis of the UHII during the most intense heatwave of the long-term climatic period, and the comparison with other heatwaves with lower intensity, revealed that UHII is mainly modulated by the predominant local/regional wind conditions, such as wind intensity and direction, rather than heatwave intensity. In fact, the highest daytime and nighttime UHII was obtained for the heatwave with the lowest intensity considered in this study. Hence, UHI adaptation and mitigation measures should consider changes in local/regional wind conditions under future climate scenarios.

CRediT authorship contribution statement

Rui Silva: Conceptualization, Methodology, Software, Data curation, Formal analysis, Investigation, Writing – original draft. **Ana Cristina Carvalho:** Formal analysis, Writing – original draft, Writing – review & editing. **Susana Cardoso Pereira:** Data curation, Writing – review & editing. **David Carvalho:** Writing – review & editing. **Alfredo Rocha:** Conceptualization, Methodology, Formal analysis, Writing – review & editing, Supervision.

Declaration of Competing Interest

The authors declare that they have no known competing financial interests or personal relationships that could have appeared to influence the work reported in this paper.

Acknowledgments

The authors acknowledge the FCT/MCTES for the financial support to CESAM (UIDP/50017/2020 + UIDB/50017/2020), through national funds. Rui Silva acknowledges the Portuguese Foundation for Science and Technology (FCT) for his PhD Grant (Refª SFRH/BD/139020/2018). Susana Cardoso Pereira acknowledges the Portuguese Foundation for Science and Technology (FCT), within the project FIREMODSAT II: Supporting FIRE-management decisions combining fire spread MODelling and SATellite data in an operational context in Portugal (part II), (Refª. PTDC/ASPSIL/28771/2017), for her research grant (Refª BI/UI88/1760/2019). David Carvalho acknowledges the Portuguese Foundation for Science and Technology (FCT) for his researcher contract (CEECIND/01726/2017).

References

Bougeault, P., Lacarrere, P., 1989. Parameterization of orography-induced turbulence in a mesobeta–scale model. Mon. Weather Rev. 117, 1872–1890. https://doi.org/10.1175/1520-0493(1989)117<1872:POOITI>2.0.CO;2.

Büttner, G., 2014. In: Manakos, I., Braun, M. (Eds.), CORINE Land Cover and Land Cover Change Products BT - Land Use and Land Cover Mapping in Europe: Practices & Trends. Springer, Netherlands, Dordrecht, pp. 55–74. https://doi.org/10.1007/978-94-007-7969-3_5.

Chen, F., Dudhia, J., 2001. Coupling an advanced land surface–hydrology model with the penn state–NCAR MM5 modeling system. Part I: model implementation and sensitivity. Mon. Weather Rev. 129, 569–585. https://doi.org/10.1175/1520-0493(2001)129<0569:CAALSH>2.0.CO;2.

Chen, F., Kusaka, H., Bornstein, R., Ching, J., Grimmond, C.S.B., Grossman-Clarke, S., Loridan, T., Manning, K.W., Martilli, A., Miao, S., Sailor, D., Salamanca, F.P., Taha, H., Tewari, M., Wang, X., Wyszogrodzki, A.A., Zhang, C., 2011. The integrated WRF/urban modelling system: development, evaluation, and applications to urban environmental problems. Int. J. Climatol. 31, 273–288. https://doi.org/10.1002/joc.2158.

Dee, D.P., Uppala, S.M., Simmons, A.J., Berrisford, P., Poli, P., Kobayashi, S., Andrae, U., Balmaseda, M.A., Balsamo, G., Bauer, P., Bechtold, P., Beljaars, A.C.M., van de Berg, L., Bidlot, J., Bormann, N., Delsol, C., Dragani, R., Fuentes, M., Geer, A.J., Haimberger, L., Healy, S.B., Hersbach, H., Hólm, E.V., Isaksen, L., Kållberg, P., Köhler, M., Matricardi, M., Mcnally, A.P., Monge-Sanz, B.M., Morcrette, J.J., Park, B.K., Peubey, C., de Rosnay, P., Tavolato, C., Thépaut, J.N., Vitart, F., 2011. The ERA-interim reanalysis: configuration and performance of the data assimilation system. Q. J. R. Meteorol. Soc. 137, 553–597. https://doi.org/10.1002/qj.828.

Diaz, S., Mock, P., Bernard, Y., Bieker, G., Pniewska, I., Ragon, P., Rodriguez, F., Tietge, U., Wappelhorst, S., 2020. European Vehicle Market Statistics Pocketbook 2020/21. Berlin.

Dudhia, J., 1989. Numerical study of convection observed during the winter monsoon experiment using a mesoscale two-dimensional model. J. Atmos. Sci. https://doi.org/10.1175/1520-0469(1989)046<3077:NSOCOD>2.0.CO;2.

Fallmann, J., Emeis, S., Suppan, P., 2014. Mitigation of urban heat stress - a modeling case study for the area of Stuttgart. Erde. 144, 202–216.

Fanger, P.O., 1970. Thermal Comfort: Analysis and Applications in Environmental Engineering. Danish Technical Press.

Farr, T.G., Rosen, P.A., Caro, E., Crippen, R., Duren, R., Hensley, S., Kobrick, M., Paller, M., Rodriguez, E., Roth, L., Seal, D., Shaffer, S., Shimada, J., Umland, J., Werner, M., Oskin, M., Burbank, D., Alsdorf, D., 2007. The shuttle radar topography mission. Rev. Geophys. 45 https://doi.org/10.1029/2005RG000183.

Feng, J.-M., Wang, Y.-L., Ma, Z.-G., Liu, Y.-H., 2012. Simulating the regional impacts of urbanization and anthropogenic heat release on climate across China. J. Clim. 25, 7187–7203. https://doi.org/10.1175/JCLI-D-11-00333.1.

Fita, L., Fernández, J., García-Díez, M., 2010. CLWRF : WRF modifications for regional climate simulation under future scenarios. Differences 1–4.

Georgescu, M., Moustaoui, M., Mahalov, A., Dudhia, J., 2011. An alternative explanation of the semiarid urban area "oasis effect". J. Geophys. Res. Atmos. 116 https://doi.org/10.1029/2011JD016720.

Giorgetta, M.A., Jungclaus, J., Reick, C.H., Legutke, S., Bo, M., Brovkin, V., Crueger, T., Esch, M., Fieg, K., Glushak, K., Gayler, V., Haak, H., Hollweg, H., Ilyina, T., Kinne, S., Kornblueh, L., Matei, D., Mauritsen, T., Mikolajewicz, U., Mueller, W., Notz, D., Pithan, F., Raddatz, T., Rast, S., Redler, R., Roeckner, E., Schmidt, H., Schnur, R., Segschneider, J., Six, K.D., Stockhause, M., Timmreck, C., Widmann, H., Wieners, K., Claussen, M., 2013. Climate and Carbon Cycle Changes from 1850 to 2100 in MPI-ESM Simulations for the Coupled Model Intercomparison Project Phase, 5 5, pp. 572–597. https://doi.org/10.1002/jame.20038.

Grell, G., Freitas, S., 2014. A scale and aerosol aware stochastic convective parameterization for weather and air quality modeling. Atmos. Chem. Phys. Dis. https://doi.org/10.5194/acp-14-5233-2014.

Hall, J.E., 2015. Guyton and Hall Textbook of Medical Physiology. Guyton Physiology, Elsevier Health Sciences.

Harman, I.N., Belcher, S.E., 2006. The surface energy balance and boundary layer over urban street canyons. Q. J. R. Meteorol. Soc. 132, 2749–2768. https://doi.org/10.1256/qj.05.185.

Hong, S., Lim, J., 2006. The WRF Single-Moment 6-Class Microphysics Scheme (WSM6). J. Korean Meteorol, Soc.

Huang, M., Gao, Z., Miao, S., Chen, F., 2019. Sensitivity of urban boundary layer simulation to urban canopy models and PBL schemes in Beijing. Meteorog. Atmos. Phys. 131, 1235–1248. https://doi.org/10.1007/s00703-018-0634-1.

Ichinose, T., Shimodozono, K., Hanaki, K., 1999. Impact of anthropogenic heat on urban climate in Tokyo. Atmos. Environ. 33, 3897–3909. https://doi.org/10.1016/S1352-2310(99)00132-6.

INE, 2018. Mobilidade e funcionalidade do território nas Áreas Metropolitanas do Porto e de Lisboa : 2017 (Lisbon).

Jiménez, P.A., Dudhia, J., González-Rouco, J.F., Navarro, J., Montávez, J.P., García-Bustamante, E., 2012. A revised scheme for the WRF surface layer formulation. Mon. Weather Rev. 140, 898–918. https://doi.org/10.1175/MWR-D-11-00056.1.

Kusaka, H., Kimura, F., 2004. Coupling a single-layer urban canopy model with a simple atmospheric model: impact on urban heat island simulation for an idealized case. J. Meteorol. Soc. Jpn. https://doi.org/10.2151/jmsj.82.67.

Kusaka, H., Kondo, H., Kikegawa, Y., Kimura, F., 2001. A simple single-layer urban canopy model for atmospheric models: comparison with multi-layer and slab models. Bound.-Layer Meteorol. 101, 329–358. https://doi.org/10.1023/A:1019207923078.

Li, X., Mitra, C., Dong, L., Yang, Q., 2018. Understanding land use change impacts on microclimate using weather research and forecasting (WRF) model. Phys. Chem. Earth, Parts A/B/C 103, 115–126. https://doi.org/10.1016/j.pce.2017.01.017.

Ma, S., Pitman, A., Hart, M., Evans, J.P., 2017. The impact of an urban canopy and anthropogenic heat fluxes on Sydney's. Climate 37, 255–270. https://doi.org/10.1002/joc.5001.

Marta-Almeida, M., Teixeira, J.C., Carvalho, M.J., Melo-Gonçalves, P., Rocha, A.M., 2016. High resolution WRF climatic simulations for the Iberian Peninsula: model validation. Phys. Chem. Earth 94, 94–105. https://doi.org/10.1016/j.pce.2016.03.010.

Martilli, A., Clappier, A., Rotach, M.W., 2002. An urban surface exchange parameterisation for mesoscale models. Bound.-Layer Meteorol. 104, 261–304. https://doi.org/10.1023/A:1016099921195.

Miguez-Macho, G., Stenchikov, G.L., Robock, A., 2004. Spectral nudging to eliminate the effects of domain position and geometry in regional climate model simulations. J. Geophys. Res. Atmos. 109 https://doi.org/10.1029/2003JD004495.

Mlawer, E.J., Taubman, S.J., Brown, P.D., Iacono, M.J., Clough, S.A., 1997. Radiative transfer for inhomogeneous atmospheres: RRTM, a validated correlated-k model for the longwave. J. Geophys. Res. Atmos. 102, 16663–16682. https://doi.org/10.1029/97JD00237.

Oke, T.R., 1988. Boundary layer climates (second edition). Q. J. R. Meteorol. Soc. 114, 1568. https://doi.org/10.1002/qj.49711448412.

Oke, T.R., Mills, G., Christen, A., Voogt, J.A., 2017. Urban Climates. Cambridge University Press, Cambridge. https://doi.org/10.1017/9781139016476.

PORDATA, 2018. Average No. of Individuals per Km^2 [WWW Document]. URL. https://www.pordata.pt/en/Municipalities/Population+density-452.

PORDATA, 2019. Electricity Consumption Per Inhabitant: Total and by Type of Consumption [WWW Document]. URL. https://www.pordata.pt/en/Municipalities/Electricity+consumption+per+inhabitant+total+and+by+type+of+consumption-435 (accessed 5.22.19).

Rocha, A., Pereira, S.C., Viceto, C., Silva, R., Neto, J., Marta-Almeida, M., 2020. A consistent methodology to evaluate temperature and heat wave future projections for cities: a case study for Lisbon. Appl. Sci. https://doi.org/10.3390/app10031149.

Ruiting, L., Han, Z., 2016. The effects of anthropogenic heat release on urban meteorology and implication for haze pollution in the Beijing-Tianjin-Hebei region. Adv. Meteorol. 2016, 1–11. https://doi.org/10.1155/2016/6178308.

Sailor, D.J., Lu, L., 2004. A Top – Down Methodology for Developing Diurnal and Seasonal Anthropogenic Heating Profiles for Urban Areas, 38, pp. 2737–2748. https://doi.org/10.1016/j.atmosenv.2004.01.034.

Sailor, D.J., Georgescu, M., Milne, J.M., Hart, M.A., 2016. Development of a National Anthropogenic Heating Database with an Extrapolation for International Cities, 118, pp. 7–18. https://doi.org/10.1016/j.atmosenv.2015.07.016.

Shiguang, M., Fei, C., 2014. Enhanced Modeling of Latent Heat Flux from Urban Surfaces in the Noah / Single-Layer Urban Canopy Coupled Model. https://doi.org/10.1007/s11430-014-4829-0.

Silva, R., Carvalho, A.C., Carvalho, D., Rocha, A., 2021. Study of urban Heat Islands using different urban canopy models and identification methods. Atmos. https://doi.org/10.3390/atmos12040521.

Skamarock, W.C., Klemp, J.B., Dudhi, J., Gill, D.O., Barker, D.M., Duda, M.G., Huang, X.-Y., Wang, W., Powers, J.G., 2008. A description of the advanced research WRF version 3. Tech. Rep. 113 https://doi.org/10.5065/D6DZ069T.

Warrach-Sagi, K., Mohr, V., Wulfmeyer, V., 2018. High resolution WRF simulations for climate change studies in Germany. In: High Performance Computing in Science And Engineering' 17: Transactions of the High Performance Computing Center, Stuttgart (HLRS), 2017, pp. 431–440. https://doi.org/10.1007/978-3-319-68394-2_25.

Yang, J., Wang, Z.-H., 2015. Optimizing urban irrigation schemes for the trade-off between energy and water consumption. Energy Build. 107, 335–344. https://doi.org/10.1016/j.enbuild.2015.08.045.

Yang, J., Fei, Z.W., Miao, S., Tewari, M., Voogt, J.A., 2015. Enhancing Hydrologic Modelling in the Coupled Weather Research and Forecasting – Urban Modelling System 87–109. https://doi.org/10.1007/s10546-014-9991-6.